Influence of the Residual Iron on the Erosion of Carbon Bricks in a 4000 m³ Blast Furnace Hearth: From the Measured Properties to the Proposed Mechanisms

GANG WANG, ZHEHAN LIAO, ZHAOWEN HU, DONGDONG WANG, HAO BAI, ZHONGPING ZOU, and JIAN XU

A blast furnace operates under a countercurrent flow process, and a wide variety of physical and chemical reactions take place, especially in the hearth at the highest temperature. Therefore, the working status and erosion of the carbon brick have a critical influence on the longevity of the blast furnace. Although the phenomena in the hearth cannot be directly observed through the black box, hearth dissection provides an alternative way to access and subsequently evaluate the internal conditions. In this paper, a 4000 m³ blast furnace hearth was dissected, and 12 residual iron samples were collected and subjected to composition, morphology, and thermal conductivity analyses. The results show that in the center of the hearth, the residual iron had thicker metallic iron strips. This is because the residual iron in the center of the dissected hearth was fully mixed with carbon or coke, and this mixing apparently enhanced the heat conductivity in the center of the hearth to as great as 80.5 W/(m K). However, such a mixing state was gradually relieved in the regions either close to the wall or settling on the bottom. Thus, the residual iron near the wall formed a needle-like surface with a layer-by-layer structure in the form of alternatively thinner strip-shaped carbon and metallic iron, and the thermal conductivities of the residual iron near the wall were above 40.0 W/(m K) regardless of the relative height. Moreover, the erosion mechanisms of the blast furnace hearth wall are proposed, and the erosion thickness is accordingly evaluated based on the heat transfer model, in which the measured thermal conductivities of the residual iron are taken into consideration. According to the erosion mechanism, the thickness of residual iron is thinner, the erosion is more serious.

GANG WANG is with the School of Metallurgical and Ecological Engineering, University of Science and Technology Beijing, Beijing 100083, P.R. China and also with the CISDI Engineering Co. Ltd., Chongqing 401122, P.R. China. ZHEHAN LIAO, ZHAOWEN HU, and DONGDONG WANG are with the College of Materials Science and Engineering, Chongqing University, Chongqing 400044, China. HAO BAI is with the School of Metallurgical and Ecological Engineering, University of Science and Technology Beijing. ZHONGPING ZOU is with the CISDI Engineering Co. Ltd. JIAN XU is with the College of Materials Science and Engineering, Chongqing University and also with the Chongqing Key Laboratory of Vanadium-Titanium Metallurgy and Advanced Materials, Chongqing University, Chongqing 400044, P.R. China. Contact e-mail: jxu@cqu.edu.cn

Manuscript submitted June 3, 2021; accepted January 7, 2022.

Article published online January 30, 2022.

I. INTRODUCTION

THE blast furnace, which is a piece of significant industrial equipment for reducing iron ores into molten iron,[1,2] has a history of thousands of years,[3] and it is still one of the most efficient and low-consumption pieces of ironmaking equipment currently used in 90 pct of molten iron production in the world.[4] On the other hand, the development of technology for large-scale blast furnace longevity is of vital importance and has received tremendous efforts worldwide.[5–7] However, due to the worst working environment, the wall of the hearth is easily eroded,[8] which directly determines the longevity of the blast furnace.[9] According to previous investigations, there are four main types of erosion of the hearth, namely, the mushroom type,[10] the elephant foot type,[11–13] the wide face type,[14] and the pot bottom type.[15] At the same time, with improvements in hearth design and refractory materials in recent decades, the elephant foot type instead of the mushroom type has

become the most common type of erosion.[16] In addition, the erosion of the hearth is mainly concentrated on carbon brick erosion, and erosion is mainly caused by hot metal scouring and erosion,[15,17–19] alkali metal erosion,[20] carbon brick ring cracking,[21] hot metal penetration,[22] etc. For the process of carbon brick erosion, Jiao et al.[23] pointed out that some protective layers were formed to protect the carbon brick, which was hardly penetrated by harmful elements. At the same time, Song et al.,[24,25] through carbon brick corrosion by hot iron molten experiments, found that the degree of loss of carbon brick mass mainly ranged from 20.0 to 30.0 pct, which confirms that carbon brick itself cannot maintain such a long production time directly in contact with hot molten iron and that some protective layer formed to protect the carbon brick.

To further illuminate the interaction between the hot metal and the wall for hearth erosion, the residual iron in the dissected hearth was subjected to scanning electron microscopy-energy dispersive spectroscopy, optical microscopy, X-ray diffraction, and Raman spectroscopy by Zhang et al.[4,26] and Shinotake et al.,[14] respectively. They studied the residual iron density and phase distribution in the radial direction. At the same time, the mechanism of sidewall erosion by the shrinkage of the viscous layer and solidified layer near bricks was preliminarily analyzed. Moreover, Nishioka et al.[27] examined basic characteristic features of drainage in a blast furnace hearth by two- and three-dimensional mathematical models, which were developed based on the finite difference method to simulate molten iron and slag flow in the hearth of a blast furnace. The results indicate that residual iron was affected by the conditions in the hearth.

Nevertheless, in previous studies, researchers have concentrated on the properties of residual iron samples in the radial direction at the same height in the hearth, and the effect of residual iron on carbon brick erosion is also unclear. Therefore, 12 residual iron samples were collected from the erosion region in the dissected hearth of a 4000 m³ blast furnace along the radial and vertical directions. The composition, morphology, and thermal conductivity analyses of these samples provide profound insight into the evolution of erosion in the blast furnace hearth. Furthermore, based on the measured thermal conductivities of the residual iron and the heat transfer model, an investigation of carbon brick erosion mechanisms was carried out.

II. SAMPLE COLLECTION

After a 4000 m³ blast furnace was cooled and iron was discharged, 12 residual iron samples were collected from the erosion region of the dissected hearth. The relative sampling locations are schematically described in Figure 1(a). Specifically, 7 samples, denoted as #1 to #7, were collected from the regions close to the center to that near the wall in the radial direction at the bottom level of the hearth. Another 5 samples, denoted as #8 to #12, were all collected at different heights in the region near the wall. For example, sample #12 was near the taphole, while sample #8 was in the gap between the carbon bricks underneath the refractory brick. In addition, the appearance of the 12 residual iron samples is demonstrated in Figure 1(b).

III. RESULTS AND DISCUSSION

A. The Composition and Density Distribution of Residual Iron Samples

During the composition analysis process, to homogenize the measurement, 12 residual iron samples were first ground into a fine powder from the different parts of the sample, and then, the powder was screened by a 200-mesh sieve. Finally, the treated samples were measured by an X-ray fluorescence (XRF) spectrometer and a carbon/sulfur analyzer at room temperature. The results along the radial and vertical directions are marked with blue and orange backgrounds, respectively, in Figure 2(a).

First, all of the residual iron samples were mainly composed of iron (minimum content 50.0 wt pct) and carbon (maximum content 47.0 wt pct). In addition, the contents of Ca, Al, and S were less than 2.0 wt pct, while that of Si was less than 10.0 wt pct. Second, in the radial direction, the content of TFe was increased from the center to the edge, and then it slightly fluctuated. In contrast, that of C was accordingly decreased and became stable in the region near the edge of the dissected hearth. To be more specific, sample #1 near the center had 49.4 wt pct TFe and 47.0 wt pct C, while the TFe content in sample #3 reached 82.6 wt pct, and the C content in sample #7 was further decreased to 15.0 wt pct. On the other hand, a fluctuation in both the TFe and C contents in the vertical direction was observed in the region close to the taphole. Third, although the distributions of other elements did not have such apparent fluctuations as TFe and C, the contents of Ca, Si, and Al jumped to as great as 1.4, 7.4, and 1.9 wt pct, respectively, in the erosion boundary close to the wall. The above results provided an important feature: the residual iron left in the center of the dissected blast furnace hearth was fully mixed with coke, and such a mixing state was gradually relieved in the regions of the hearth either close to the wall or settling on the bottom. The highlighted feature was further validated by the apparent density measurement results of the samples in Figure 2(b). The drainage method was used for the density measurement. This method obtained the density using the relationship between the mass and volume of the sample, and the calculation formula is as follows:

$$\rho = \frac{m}{v_2 - v_1} \qquad [1]$$

where ρ represents the density of the sample and m represents the mass of the sample. v_2 and v_1 denote the volume of the sample after and before being placed into the measuring cylinder filled with water, respectively.
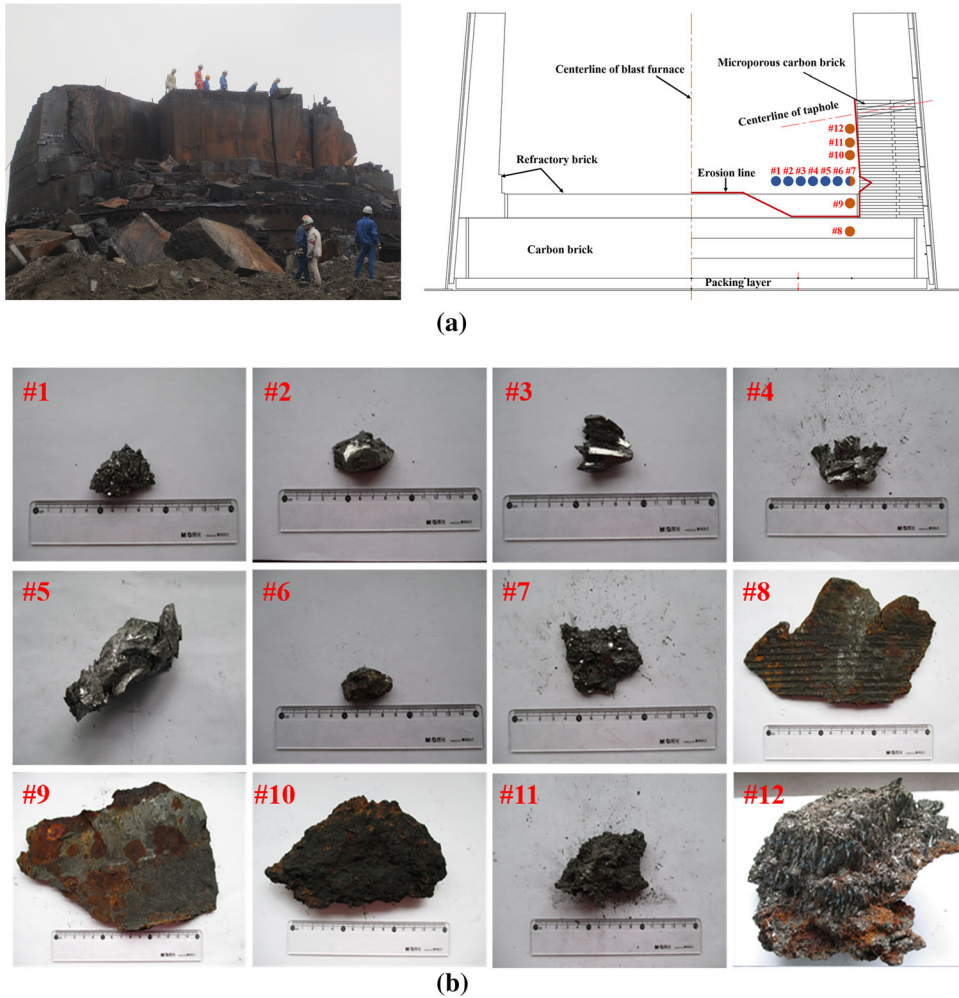
(a)

(b)

Fig. 1—(*a*) Schematic diagram of the relative sampling locations of the 12 residual iron samples in the dissected blast furnace hearth with (*b*) individual appearances.

In the radial direction, the sample density was increased from approximately 4.2 g/cm^3 (sample #1 near the center) to as great as 5.3 g/cm^3 (sample #4 close to the wall). The density of sample #6 was 3.0 g/cm^3, which was attributed to its porous structure. In addition, the density of the residual iron in the vertical direction decreased from 6.4 g/cm^3 (sample #8 at the bottom) to approximately 5.1 g/cm^3 (sample #12 at the top). Overall, except for some samples with porous structures (for example, sample #6), the apparent density distribution had a roughly inverse relationship with the carbon content in the residual iron. Consequently, more efforts were devoted to further clarify the differences in the iron and carbon morphology of the residual iron samples between the central and near-wall regions.

B. *Further Comparison of the Residual Iron Samples #5 and #12*

Samples #5 and #12 were carefully selected due to their similarities in both composition and density but difference in sampling location. Specifically, sample #5, which was collected from the center bottom of the dissected hearth, had 80.7 wt pct TFe and 13.8 wt pct C

with an apparent density of 4.7 g/cm^3. In contrast, sample #12, collected from the region near the wall and close to the taphole, had 73.6 wt pct TFe and 13.9 wt pct C with an apparent density of 5.1 g/cm^3.

The appearance of the above two samples was first compared in Figure 3(a). As schematic diagrams in the corresponding insets show, sample #5 had a smooth shape with sharp edges, and part of the sample's surface had a metallic luster. In contrast, sample #12 was quite rough with a needle-like surface, and a layer-by-layer structure was observed. Both samples were then polished and subjected to optical microscope observation. Each photo was taken at ×25 magnification, and a bird's-eye view was obtained by stitching these photos together in Figure 3(b). The bright strips represent metallic iron, while the dark areas represent carbon. Moreover, a pearlite structure was observed in sample #12. The results agreed with the energy-dispersive spectroscopy (EDS) elemental mapping in Figure 3(c). There were two distinct morphological features between the two samples. First, the metallic iron strips in sample #5 were much thicker than their counterparts in sample #12. Second, the bulky carbon accordingly occupied the space between the strips in sample #5, while the
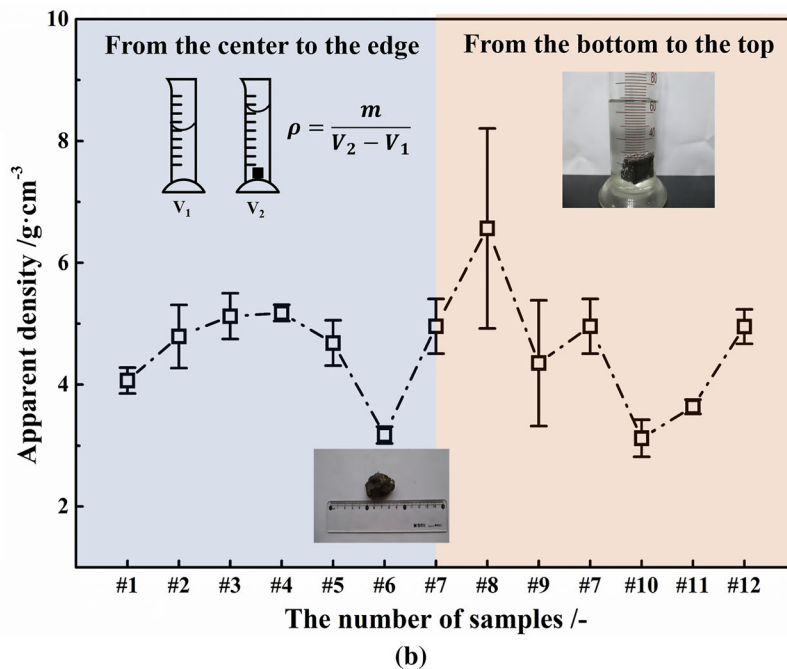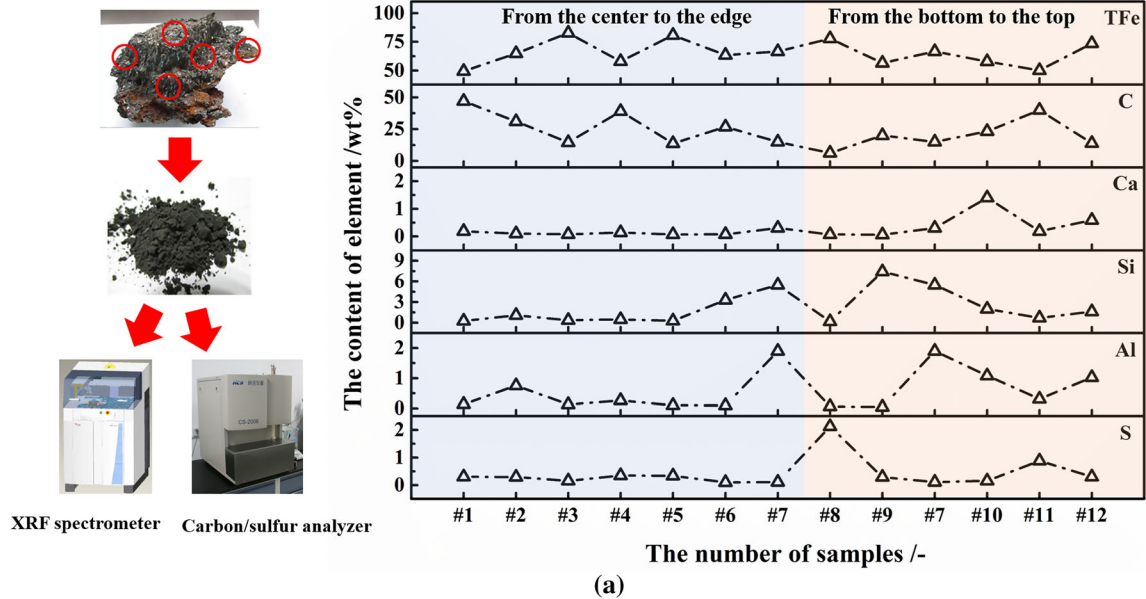
Fig. 2—The attributes of the 12 residual iron samples. (*a*) the elemental composition distributions results and (*b*) the apparent density in either radial (left marked with blue) or vertical (right marked with orange) direction (Color figure online).

strip-shaped carbon and metallic iron together formed the alternative layer-by-layer distribution in sample #12, which supported its appearance, as mentioned above.

C. *The Thermal Conductivity Distribution of Residual Iron Samples*

Except for samples #3 and #6, which were quite porous and easy to break, the other samples were made into short columns with a 12.5 mm diameter and 2.0 mm thickness and then subjected to thermal conductivity measurements by the laser flash technique at room temperature. More details, measurement samples were

taken from three different parts of the residual iron sample, and the average value was used as the thermal conductivity of the sample. The results are compared in Figure 4.

In the radial direction, sample #1 in the region close to the center of the hearth had excellent thermal conductivity (80.5 W/(m K)), and the result was decreased by nearly half in the region near the wall. For example, the thermal conductivity of sample #7 was approximately 45.0 W/(m K). On the other hand, except for samples #9 and #10, the thermal conductivity of the residual iron in the vertical direction fluctuated between 52.7 and 42.0 W/(m K). Meanwhile, the slag
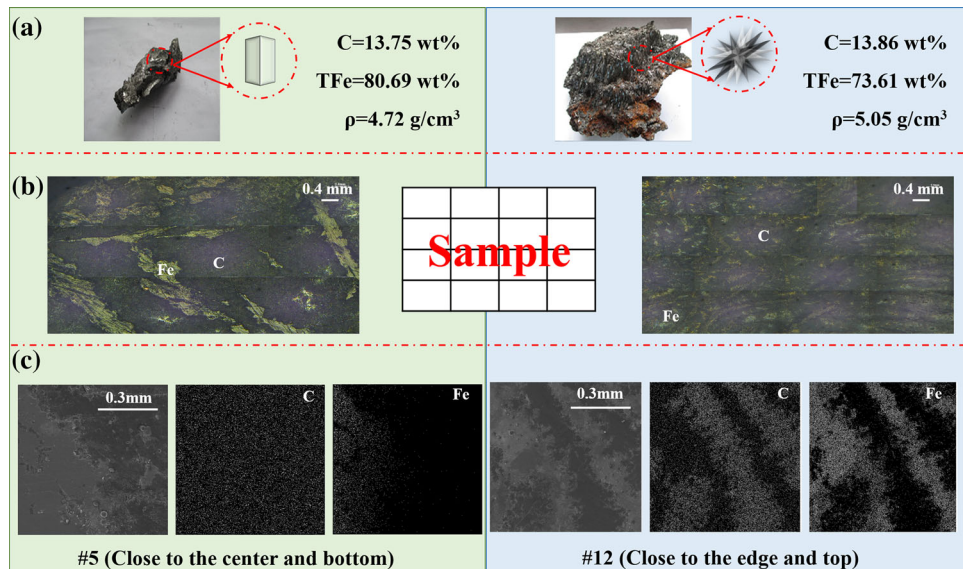
Fig. 3—Comparison of (*a*) the appearance and morphology *via* (*b*) the optical microscope and (*c*) the EDS elemental mapping between samples #5 (with green background) and #12 (with blue background) (Color figure online).
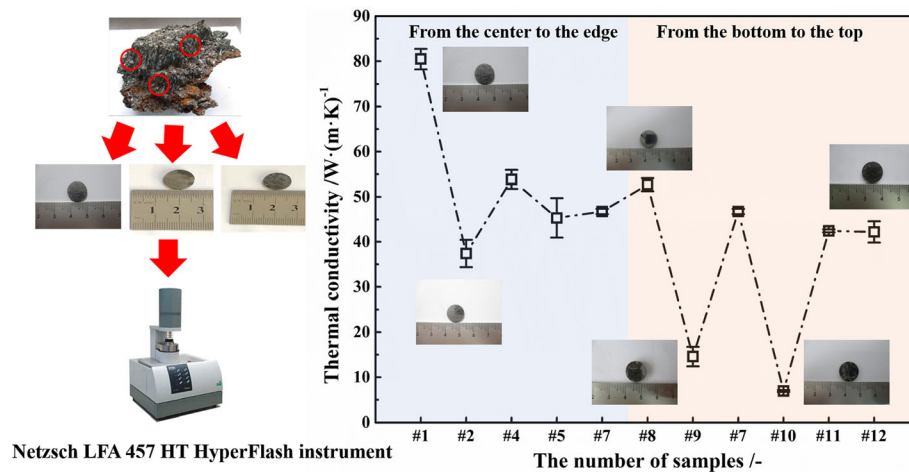

Fig. 4—Comparison of the thermal conductivity between different samples.

composition in samples #9 and #10 significantly decreased the thermal conductivity to as small as 6.9 W/(m K). Therefore, the bulky carbon in the residual iron enhanced the heat conductivity in the central region of the blast furnace hearth, while the thermal conductivity in the region close to the wall was decreased and stabilized above 40.0 W/(m K) regardless of the relative height, and the mixed slag with Ca and Si was able to significantly decrease the thermal conductivity of the residual iron.

D. *The Proposed Erosion Mechanisms of Residual Iron on the Carbon Brick*

To quantitatively evaluate the influence of the residual iron on the erosion of the carbon brick in the blast furnace hearth, an erosion mechanism was proposed based on the heat transfer phenomena. Specifically, the

model consists of three layers, namely, the residual iron layer, the embrittlement layer, and the carbon brick layer, as shown in Figure 5(a). The residual iron layer was in direct contact with molten iron, and the temperature of molten iron was supposed to be 1490 °C. Then, since the exact length of residual iron was hard to measure, the thickness of the residual iron layer was assumed to be 500 mm, and the thermal conductivity was equally distributed according to the measured value. In the dissected blast furnace hearth, a 200 to 500 mm length embrittlement layer can be found on the hot surface of the carbon bricks. In addition, the iron content in the hot surface of the embrittlement layer was approximately 12.38 pct, the iron content decreased rapidly in the direction of the furnace wall, and the iron infiltration in the cold surface of the embrittlement layer was only approximately 1.6 pct. Figure 5(a) also shows the iron content changes from the inner part of the
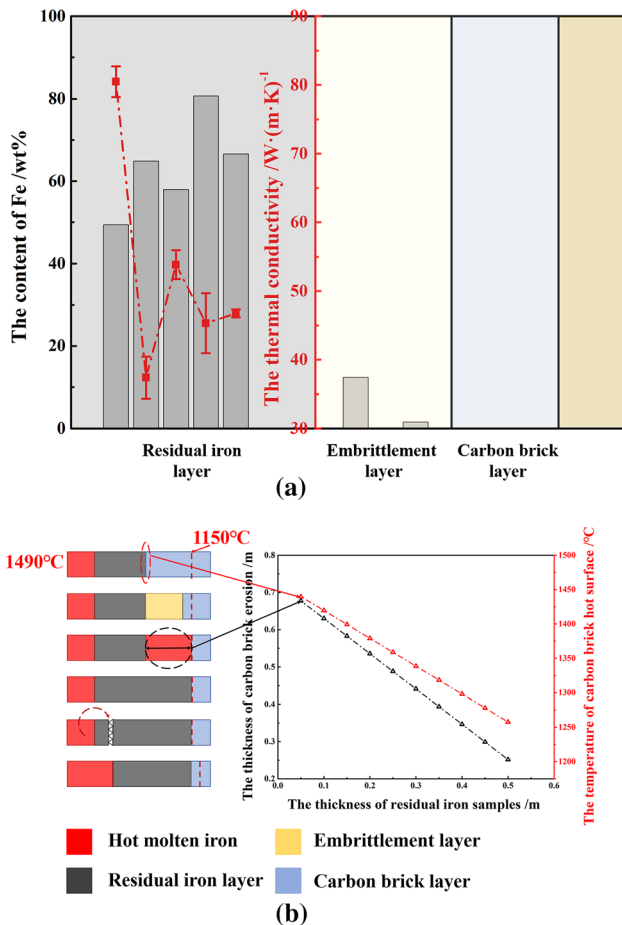
Fig. 5—The carbon bricks erosion mechanism. (*a*) the composition of the erosion model, and the iron content changes from the inner of the hearth to the wall of the blast furnace. (*b*) the schematic diagram of the erosion mechanism, and the relationship between the erosion thickness and the carbon bricks hot surface temperature with the different thickness of the residual iron samples.

hearth to the wall of the blast furnace. Moreover, we also made some extra assumptions. First, the solidification temperature of the molten iron was 1150 °C. In addition, the influence of chemical reactions in the hearth on carbon brick erosion was ignored.

Figure 5(b) presents an illustration of a hypothesis of the hearth erosion process. In the early stage of blast furnace production, a residual iron layer would be formed in front of the carbon brick layer due to the effect of the cooling stave. The formed residual iron played the role of isolation between slag, molten iron, and carbon brick. Then, as molten iron continuously eroded the residual iron, the temperature of the hot surface of the carbon brick continuously increased. This resulted in a large temperature contrast between the hot and cool surfaces of carbon brick. Then, due to the unsteady thermal stress, carbon brick ring cracks[28,29] appeared on the hot surface of the carbon brick, and an embrittlement layer was formed. With the continuous increase of the carbon brick temperature, the embrittlement layer was quickly destroyed, and hot molten iron imminently occupied the position of the embrittlement layer, which accelerated the erosion of carbon bricks.

This process ended when the hot surface temperature of carbon brick dropped to the solidification temperature of molten iron at 1150 °C. When the temperature of the hot surface of the carbon brick reached 1150 °C, the entering molten iron cooled, and graphite precipitated. Then, a new iron coagulation layer was formed. To date, carbon bricks have eroded by approximately 0.25 m. However, with the increased thermal circulation in the hearth, the residual iron would be broken out, resulting in a further rise in the hot surface temperature of carbon bricks. The process described above will be repeated, and the carbon brick gradually erodes and weakens.

However, the thickness of residual iron was hardly measured in the hearth and directly affected the erosion thickness of carbon bricks. Thus, through the heat transfer calculation, Figure 5(b) also compares the erosion thickness at the first circle erosion stage and the carbon brick hot surface temperature when the carbon brick starts to erode stage with different lengths of residual iron samples. First, the erosion thickness and carbon brick hot surface temperature are inversely proportional to the thickness of residual iron, and both have a linear relationship. Then, when the thickness of residual iron is 0.05 m, the erosion thickness and carbon brick hot surface temperature can reach 0.67 m and 1440 °C, respectively, while when the thickness of residual iron is 0.5 m, the erosion thickness and carbon brick hot surface temperature are only 0.25 m and 1257 °C, respectively.

IV. CONCLUSION

In order to analysis the effect of residual iron for the carbon brick erosion. Twelve residual iron samples were collected from the dissected hearth of a 4000 m³ blast furnace, and they were subjected to composition, density, morphology, and thermal conductivity measurements in either radial or vertical directions. An erosion mechanism was determined based on the heat transfer model and the measured thermal conductivities. The main findings could be highlighted as follows:

1. Although the residual iron samples were mainly composed of iron (minimum content of 50.0 wt pct) and carbon (maximum content of 47.0 wt pct), that left in the central dissected hearth was fully mixed with carbon or coke, and such a mixing state was gradually relieved in the regions either close to the wall or settling on the bottom.
2. Although the concentrations of the compositions were similar, the residual iron in the center of the hearth had thicker metallic iron strips, while that near the wall formed a needle-like surface with a layer-by-layer structure in the form of alternatively thinner strip-shaped carbon and metallic iron.
3. The bulky carbon mixed in the residual iron apparently enhanced the heat conductivity in the center of the hearth to as great as 80.5 W/(m K), while the thermal conductivity of the residual iron near the wall was above 40.0 W/(m K) regardless of the relative height. However, the mixing of slag intended to

significantly decrease the conductivity to as small as 6.9 W/(m K).

4. During the carbon brick erosion process, residual iron was first formed in front of the carbon bricks, and hot molten iron continuously eroded the residual iron. As the temperature of the hot surface of the carbon bricks continuously increased, an embrittlement layer was formed until it was destroyed. Then, the hot molten iron entered the destroyed carbon brick and formed a new iron coagulation layer to protect the carbon bricks. However, due to the thermal circulation of the hot molten in the hearth, the residual iron layer will be broken. The hot surface of carbon bricks will erode again, and this process will occur in a circle. Moreover, the erosion thickness and carbon brick hot surface temperature are inversely proportional to the thickness of residual iron, and both have a linear relationship. When the thickness of residual iron is 0.05 m, the erosion thickness and carbon brick hot surface temperature can reach 0.67 m and 1440 °C, respectively, while when the thickness of residual iron is 0.5 m, the erosion thickness and carbon brick hot surface temperature are only 0.25 m and 1257 °C, respectively.

ACKNOWLEDGMENTS

CONFLICT OF INTEREST

On behalf of all authors, the corresponding author states that there is no conflict of interest.

REFERENCES

1. L.L. Jiao, S.B. Kuang, L.L. Liu, A.B. Yu, Y.T. Li, X.M. Mao, and H. Xu: *Metall. Mater. Trans. B*, 2021, vol. 52B(1), pp. 138–55.
2. S.B. Kuang, Z.Y. Li, and A.B. Yu: *Steel Res. Int.*, 2018, vol. 89(1), p. 1700071.
3. X.B. Yu and Y.S. Shen: *Metall. Mater. Trans. B*, 2020, vol. 51B(5), pp. 2079–94.
4. L. Zhang, J.L. Zhang, K.X. Jiao, and C. Wang: *ISIJ Int.*, 2020, vol. 60(8), pp. 1655–61.
5. F.M. Zhang: *J. Iron Steel Res. (Int.)*, 2013, vol. 20(9), pp. 53–60.
6. J.F. Ma, H.B. Zhao, and S.S. Chen: *J. Iron Steel Res. (Int.)*, 2009, vol. 16(5), pp. 859–63.
7. T.J. Park, K.H. Ko, J.H. Lee, S. Gupta, V. Sahajwalla, and B.C. Kim: *Metall. Mater. Trans. B*, 2020, vol. 51B(3), pp. 1282–88.
8. L. Zhang, J.L. Zhang, K.X. Jiao, X.K. Zhang, S.J. Duan, X. Wu, and J.C. Wang: *Metall. Res. Technol.*, 2021, vol. 118(4), p. 410.
9. M. Naito, K. Takeda, and Y. Matsui: *ISIJ Int.*, 2015, vol. 55(1), pp. 7–35.
10. A. Preuer, J. Winter, and H. Hiebler: *Steel Res.*, 1992, vol. 63(4), pp. 139–46.
11. H. B. Zhao, S. S. Chen, J. F. Zhu, H. W. Pan, Z. J. Wang, and J. S. Sun: *5th International Congress on the Science and Technology of Ironmaking, ICSTI 2009*, 2009, pp. 897–901.
12. L. Zhang, J.L. Zhang, K.X. Jiao, G. Jia, J.T. Gong, X.T. Yang, M.X. Zhao, and W.B. Duan: *Metall. Res. Technol.*, 2021, vol. 118(1), p. 106.
13. P.C. Lai, S.W. Du, S.H. Liu, and W.T. Cheng: *Thermal Sci. Eng. Prog.*, 2021, vol. 23, p. 100908.
14. A. Shinotake, H. Nakamura, N. Yadoumaru, Y. Morizane, and M. Meguro: *ISIJ Int.*, 2003, vol. 43(3), pp. 321–30.
15. L. Shao and H. Saxén: *Steel Res. Int.*, 2012, vol. 83(9), pp. 878–85.
16. M.F. Barbés, R. Marinas, E. Brandaleze, R. Parra, and R. Colás: *ISIJ Int.*, 2008, vol. 48(2), p. 134.
17. C.E. Huang, S.W. Du, and W.T. Cheng: *ISIJ Int.*, 2008, vol. 48(2008), pp. 1182–87.
18. X.F. Dong and P. Zulli: *Ironmak. Steelmak.*, 2020, vol. 47(3), pp. 307–15.
19. X.F. Dong, P. Zulli, and M. Biasutti: *Ironmak. Steelmak.*, 2019, vol. 47(5), pp. 1–6.
20. X.F. Wang and Q.J. Zhai: *J. Iron Steel Res. (Int.).*, 2017, vol. 24(10), pp. 1016–22.
21. Q. Niu, S.S. Cheng, W.X. Xu, and W.J. Niu: *ISIJ Int.*, 2019, vol. 59(10), pp. 1776–85.
22. S.N. Silva, F. Vernilli, S.M. Justus, O.R. Marques, A. Mazine, J.B. Baldo, E. Longo, and J.A. Varela: *Ironmak. Steelmak.*, 2013, vol. 32(6), pp. 459–67.
23. K.X. Jiao, C. Wang, J.L. Zhang, S. Ren, and E. Dian-Yu: *JOM*, 2020, vol. 72(5), pp. 1935–42.
24. M.S. Song and Z.J. Yu: *Res. Iron Steel*, 2009, vol. 37(2), pp. 1–6.
25. M.S. Song, Z.Q. Zou, and Z.J. Yu: *China Metall.*, 2005, vol. 15(11), pp. 6–10.
26. L. Zhang, J.L. Zhang, K.X. Jiao, Z.P. Zou, and Y.J. Zhao: *ISIJ Int.*, 2019, vol. 59(11), pp. 1991–96.
27. K. Nishioka, T. Maeda, and M. Shimizu: *ISIJ Int.*, 2005, vol. 45(5), pp. 669–76.
28. K.X. Jiao, J.L. Zhang, Z.J. Liu, Z.Z. Liu, Y. Deng, and X.Y. Fan: *Metall. Res. Technol.*, 2018, vol. 115(1), p. 109.
29. H.B. Zhao, S.F. Huo, and S.S. Cheng: *Int. J. Miner. Metall. Mater.*, 2013, vol. 20(4), pp. 345–53.